

# Anomalous magnetic exchange in a dimerized quantum-magnet composed of unlike spin species - supplemental information

S. P. M. Curley,<sup>1</sup> B. M. Huddart,<sup>2</sup> D. Kamenskyi,<sup>3,4</sup> M. J. Coak,<sup>1</sup> R. C. Williams,<sup>1</sup> S. Ghannadzadeh,<sup>5</sup> A. Schneider,<sup>6</sup> S. Okubo,<sup>4</sup> T. Sakurai,<sup>4</sup> H. Ohta,<sup>4</sup> J. P. Tidey,<sup>7</sup> D. Graf,<sup>8</sup> S. J. Clark,<sup>2</sup> S. J. Blundell,<sup>5</sup> F. L. Pratt,<sup>9</sup> M. T. F. Telling,<sup>9</sup> T. Lancaster,<sup>2,\*</sup> J. L. Manson,<sup>10,†</sup> and P. A. Goddard<sup>1,‡</sup>

<sup>1</sup>*Department of Physics, University of Warwick, Gibbet Hill Road, Coventry, CV4 7AL, UK*

<sup>2</sup>*Centre for Materials Physics, Department of Physics, Durham University, Durham DH1 3LE, United Kingdom*

<sup>3</sup>*Experimental Physics V, Center for Electronic Correlations and Magnetism, Institute of Physics, University of Augsburg, 86135 Augsburg, Germany*

<sup>4</sup>*Molecular Photoscience Research Center, Kobe University, 657-8501 Kobe, Japan*

<sup>5</sup>*Department of Physics, Clarendon Laboratory, Oxford University, Parks Road, Oxford, OX1 3PU, UK*

<sup>6</sup>*Experimental Physics VI, Center for Electronic Correlations and Magnetism, Institute of Physics, University of Augsburg, 86135 Augsburg, Germany*

<sup>7</sup>*Department of Chemistry, University of Warwick, Gibbet Hill, Coventry CV4 7AL, U.K*

<sup>8</sup>*National High Magnetic Field Laboratory, Florida State University, Tallahassee, Florida 32310, USA*

<sup>9</sup>*ISIS Facility, Rutherford Appleton Laboratory, Chilton, Oxfordshire, OX11 0QX, UK*

<sup>10</sup>*Department of Chemistry and Biochemistry, Eastern Washington University, Cheney, Washington 99004, USA*

## EXPERIMENTAL DETAILS

### Synthesis and structure

A crystal of dimensions 0.48 x 0.32 x 0.14 mm was affixed to a 50  $\mu\text{m}$  Mitigen micromount using Fomblin-Y perfluoroether. Data were collected using a Rigaku Oxford Diffraction XtalLAB Synergy, Dualflex diffractometer [1] equipped with a HyPix-6000HE Hybrid Photon Counting area detector and employing Mo  $K_{\alpha}$  radiation ( $\lambda = 0.71073 \text{ \AA}$ ), generated by a PhotonJet, micro-focus sealed X-ray tube. Data were collected to  $d_{\text{min}} = 0.50 \text{ \AA}$ , indexed and reduced using CrysAlisPro [2] and absorption corrected for by Gaussian integration over a multifaceted crystal model.

Structural solution was performed by direct methods using SHELXS and refinement performed using SHELXL [3], implemented through Olex2. H-atoms were located from the difference map and restraints placed on the O—H 1,2- and the H—O—H 1,3-distances to maintain reasonable geometry while allowing geometric freedom with respect to the M-O bond. Non-H atom atomic displacements were treated anisotropically with those of hydrogen atoms were treated isotropically and riding on the donor atom. While the Flack parameter refined to essentially zero, the potentially inversion twin law has been retained for the purpose of discussion. Table SI shows the details of the data reduction and structure solution.

## Magnetometry

### SQUID magnetometry

SQUID magnetometry measurements were performed using a Quantum Design MPMS-XL SQUID magnetometer. Single-crystals were orientated such that the crystallographic  $a$ -axis was aligned parallel and perpendicular to the applied magnetic field  $H$ . Samples were mounted inside a gelatin capsule and held in place with a small application of Apiezon vacuum M-grease. The capsule was then mounted inside a low magnetic background drinking straw and loaded into the sample chamber. The temperature dependence of the molar susceptibility  $\chi$  was obtained in the linear limit using the relation  $\chi = M/nH$  where  $M$  is the measured magnetic moment and  $n$  is the number of moles of the compound.

### Radio frequency susceptometry

The dynamic magnetic susceptibility ( $dM/dH$ ) was measured using as radio-frequency (RF) oscillator circuit technique. The set-up involves a RF circuit and a Tunnel-Diode oscillator (TDO) and is based on an LCR circuit. A single-crystal was placed within a small detector coil with applied field orientated parallel then perpendicular to the crystallographic  $a$ -axis. The detector coil is inductively coupled to the TDO which measures changes in the oscillation frequency ( $\Delta\omega$ ) of the circuit. This can be related to the real part of the dynamic susceptibility,

$$\frac{\Delta\omega}{\omega} = -\pi f \frac{dM}{dH} \quad (1)$$

TABLE SI. Single crystal X-ray data and refinements details for  $\text{CuVOF}_4(\text{H}_2\text{O})_6 \cdot \text{H}_2\text{O}$ .

Parameter (units)	Fit Results (error)
Instrument	Rigaku Oxford Diffraction Synergy S
Method	Single crystal
Empirical formula	$\text{Cu F}_4 \text{H}_{14} \text{O}_8 \text{V}$
Formula weight ( $\text{g mol}^{-1}$ )	332.59
Temperature (K)	150.00(10)
Crystal system	orthorhombic
Space group	$Pna2_1$
$a$ ( $\text{\AA}$ )	15.65164(16)
$b$ ( $\text{\AA}$ )	8.24054(8)
$c$ ( $\text{\AA}$ )	7.37877(7)
$\alpha$ ( $^\circ$ )	90
$\beta$ ( $^\circ$ )	90
$\gamma$ ( $^\circ$ )	90
Volume ( $\text{\AA}^3$ )	951.699(16)
Z	4
$\rho_{\text{calc}}$ ( $\text{g cm}^{-3}$ )	2.321
$\mu$ ( $\text{mm}^{-1}$ )	3.301
Crystal size ( $\text{mm}^3$ )	$0.479 \times 0.320 \times 0.143$
Radiation	Mo $\text{K}_\alpha$ ( $\lambda = 0.71073$ )
$2\theta$ range for data collection ( $^\circ$ )	7.18 to 89.88
$h$ -index range	$-31 \leq h \leq 31$
$k$ -index range	$-14 \leq k \leq 16$
$l$ -index range	$-14 \leq l \leq 14$
Reflections collected	37584
Independent reflections	7743
Data/restraints/parameters	7743/22/171
Goodness-of-fit on F2	1.069
Final R indexes [ $I \geq 2\sigma(I)$ ]	$R_1 = 0.0226$ $wR_2 = 0.0602$
Final R indexes [all data]	$R_1 = 0.0232$ $wR_2 = 0.0604$
Largest diff. peak/hole ( $\text{e \AA}^{-3}$ )	0.78/-1.10
Flack parameter	0.012(5)

where  $f$  is the filling factor [4, 5]. The detector-coil and TDO were mounted into a top-loading liquid sorption pumped  $^3\text{He}$  cryostat. Fields of up to 35 T were obtained by utilising a DC-field resistive magnet located in Cell-12 at the National High Magnetic Field Laboratory, Florida, US. Empty-coil field sweeps were collected as a background and subtracted from similar temperature total frequency responses in order to isolate the sample response.

## Electron-spin resonance

Electron-spin resonance (ESR) experiments were performed over wide ranges of frequencies (9 – 500 GHz), magnetic fields (up to 15 T) and temperatures (2 – 295 K). The low-frequency ESR studies were performed on single-crystals of  $\text{CuVOF}_4(\text{H}_2\text{O})_6 \cdot \text{H}_2\text{O}$  using a commercially available X-Band Bruker ESR spectrometer operating at 9.35 GHz at Augsburg University. High-frequency ESR experiments were done using a multi-frequency spectrometer operated in combination with a 16 T pulsed magnet (5 msec pulse) at Kobe University (Japan). Backward Wave Oscillators and Gunn Diodes were employed as sources of mm- and submm-wavelength radiation. 2,2-Diphenyl-1-picrylhydrazyl (DPPH) was used as a standard magnetic field marker with  $g$ -factor  $g = 2.0036$ .

## Muon-spin relaxation

Zero-field (ZF) and longitudinal field (LF) muon-spin relaxation ( $\mu^+\text{SR}$ ) measurements [6, 7] were made on a polycrystalline sample of  $\text{CuVOF}_4(\text{H}_2\text{O})_6 \cdot \text{H}_2\text{O}$  using the HiFi spectrometer at the ISIS facility, Rutherford Appleton Laboratory, UK. In a  $\mu^+\text{SR}$  experiment [6, 7] spin polarized muons are implanted into the sample, where they precess about the total magnetic field  $B$  at the muon site at a frequency  $\nu = \gamma_\mu B/2\pi$ , where  $\gamma_\mu$  is the muon gyromagnetic ratio ( $= 2\pi \times 135.5 \text{ MHz T}^{-1}$ ). These muons decay with an average lifetime of 2.2  $\mu\text{s}$  into two neutrons and a positron. Due to the parity-violating nature of the weak interaction, positrons are emitted preferentially along the instantaneous muon spin direction. Recording the direction of emitted positron therefore allows us to infer the muon spin polarization at the time of decay. The quantity of interest is the asymmetry

$$A(t) = \frac{N_F(t) - \alpha N_B(t)}{N_F(t) + \alpha N_B(t)}, \quad (2)$$

where  $N_{F/B}$  is the number of positrons detected in the forward/backward detectors and  $\alpha$  is an experimental calibration constant. The asymmetry  $A(t)$  is proportional to the spin polarization of the muon ensemble.

For a magnetically-ordered compound one observes oscillations in the asymmetry  $A(t)$ . For a distribution of magnetic fields the spins will each precess at a different frequency, resulting in a relaxation of the muon polarization. When dynamics are present in the fast fluctuation limit [8, 9], the relaxation rate is expected to vary as  $\lambda \propto \Delta^2\tau$ , where  $\Delta = \sqrt{\gamma_\mu^2 \langle (B - \langle B \rangle)^2 \rangle}$  is the second moment of the local magnetic field distribution at the muon site and  $\tau$  is the correlation time. In an LF  $\mu^+\text{SR}$  experiment a field is applied parallel to the direction of the initial muon spin. Being parallel to the muon spin,

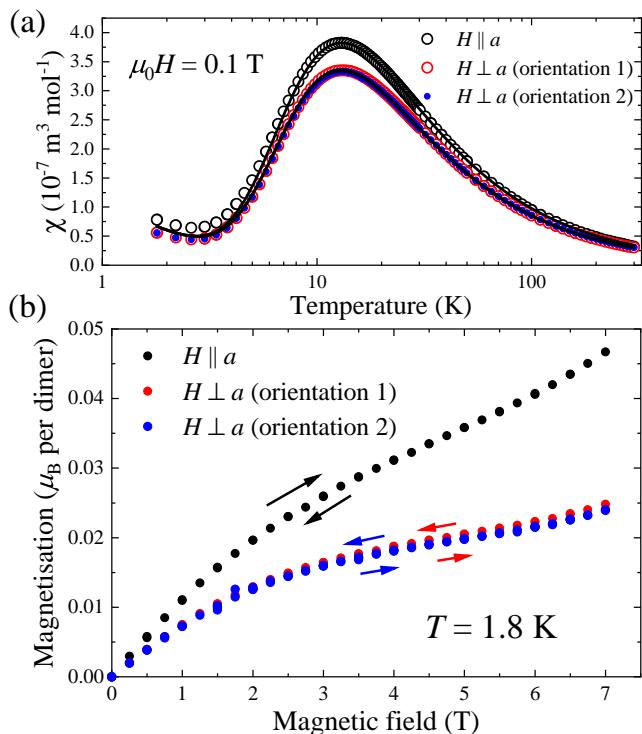


FIG. S1. Orientation dependent SQUID magnetometry for  $\text{CuVOF}_4(\text{H}_2\text{O})_6 \cdot \text{H}_2\text{O}$  with field along three orthogonal crystal directions for the magnetic susceptibility plotted as a function of temperature (a) and magnetic moment plotted as a function of applied magnetic field (b). Solid lines in (a) are fits to Eq. 3.

the applied field does not result in precession but instead ‘locks in’ the spin direction of the muon, since a large field component lies along the initial muon polarization direction. This allows us to probe the dynamics of the system, with time-varying magnetic fields at the muon site being able to flip muon spins.

## RESULTS

### Magnetometry

The results of SQUID magnetometry measurements performed on an orientated single-crystal of  $\text{CuVOF}_4(\text{H}_2\text{O})_6 \cdot \text{H}_2\text{O}$  are shown in Fig. S1. The magnetic susceptibility  $\chi(T)$  shows little difference between measurements made with the field along the two orthogonal directions for  $H \perp a$ , whilst the hump in  $\chi(T)$  for  $H \parallel a$  has a slightly larger amplitude. All datasets were

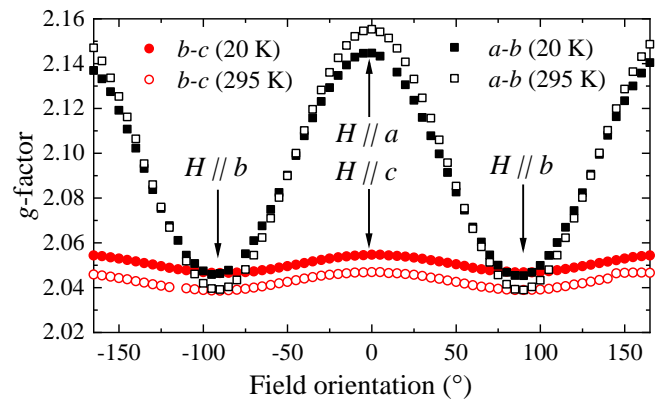


FIG. S2. The angular dependence of the  $g$ -factor of the transitions within the excited triplet state ( $S = 1$ ) in  $\text{CuVOF}_4(\text{H}_2\text{O})_6 \cdot \text{H}_2\text{O}$ .

fit to an interacting dimer model of the form,

$$\chi = (1 - \rho) \frac{N_A (g\mu_B)^2}{k_B T (3 + \exp(J_0/T) + nJ'/T)} + \rho \frac{(g_p\mu_B)^2 N_A \mu_0 S(S+1)}{3k_B T} \quad (3)$$

where here  $N_A$  is Avogadro’s number,  $\mu_B$  is the Bohr magneton,  $\mu_0$  is the permeability of free space,  $J_0$  is the intradimer exchange constant,  $J'$  is the interdimer exchange constant and  $n$  the number of nearest dimer neighbors. The second half of the equation models the low-temperature upturn in  $\chi(T)$  as an ensemble of free  $S = 1/2$  ions with an isotropic  $g$ -factor of  $g_p = 2$  with the parameter  $\rho$  capturing the fraction of the sample attributable to isotropic  $S = 1/2$  ions. As described in the main text,  $\chi(T)$  datasets were fit simultaneously with only  $g$ -factors free to vary for each dataset (resultant fit parameters can be found in the main text).

Magnetisation  $M(H)$  for field along all three orthogonal crystal directions each possess the same qualitative  $M(H)$  profile. No hysteretic behaviour is seen along any direction, indicating an absence of any ferrimagnetism in the system. For  $H \parallel a$ ,  $M(H)$  rises more rapidly than for  $H$  along the other two orthogonal orientations. This may indicate the presence of a DM vector orientated slightly along the  $a$ -axis.

### Electron-spin resonance

Angular dependencies of the triplet transitions  $g$ -factor were measured at 20 and 295 K when these transitions are dominate in the spectrum. The results are shown in Fig. S2. Apart the anisotropy of the  $g$ -factor, we also observe significant anisotropy of the EPR linewidth, which becomes much narrow when field is along the  $b$ -axis.

### Muon-spin relaxation

Zero field measurements were made on  $\text{CuVOF}_4(\text{H}_2\text{O})_6 \cdot \text{H}_2\text{O}$  for  $0.1 \leq T \leq 1.5$  K. Example spectra at three different temperatures are shown in Fig. S3. The spectra do not show any oscillations in the asymmetry, that would be characteristic of magnetic order, down to 0.1 K. These spectra were fit to a stretched exponential function

$$A(t) = A_1 e^{-\lambda_1 t} + A_2 e^{-\lambda_2 t}, \quad (4)$$

where the component with amplitude  $A_1$  and relaxation rate  $\lambda_2$  is due to muons that are sensitive to fluctuating electronic moments. A slowly-relaxing component with amplitude  $A_2$  and  $\lambda_2$  has contributions from several sources: muons that stop in the silver sample holder or cryostat tails, or from muons stopping in the sample, but at positions where they are not sensitive to the electronic moments. The amplitudes  $A_1$  and  $A_2$  reflect the proportion of muons stopping in each of the distinct magnetic environments and were found not to vary significantly with temperature, so were fixed to their average values 3.35% and 18.7% respectively in the fitting procedure. As shown in Fig. S3, there is no significant change in the shape of the spectra with changing temperature. The relaxation parameters obtained from a fitting of the above form at each temperature are shown in Fig. S4 and also show little temperature dependence.

We also carried out longitudinal field (LF) measurements at  $T = 1.2$  K for  $0.5 \leq B \leq 2000$  mT. Example spectra at two different fields are shown in Fig. S5. We

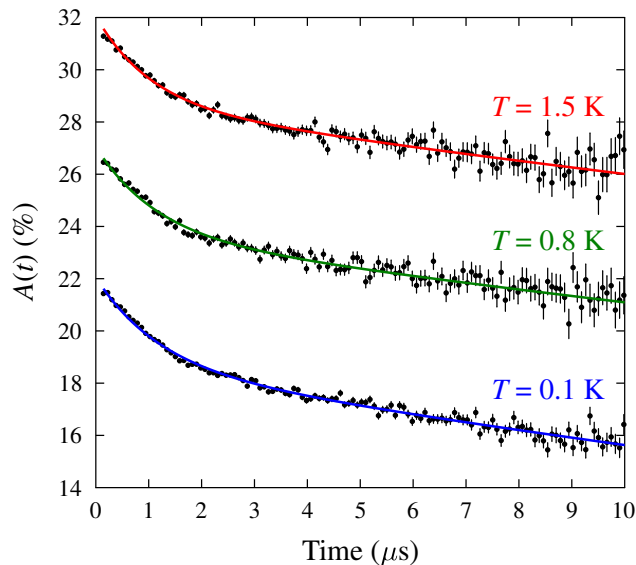


FIG. S3. Zero field  $\mu^+$ SR spectra for  $\text{CuVOF}_4(\text{H}_2\text{O})_6 \cdot \text{H}_2\text{O}$  at three different temperatures. For clarity, we show  $A(t) + 5\%$  and  $A(t) + 10\%$  for the data at  $T = 0.8$  K and  $T = 1.5$  K, respectively.

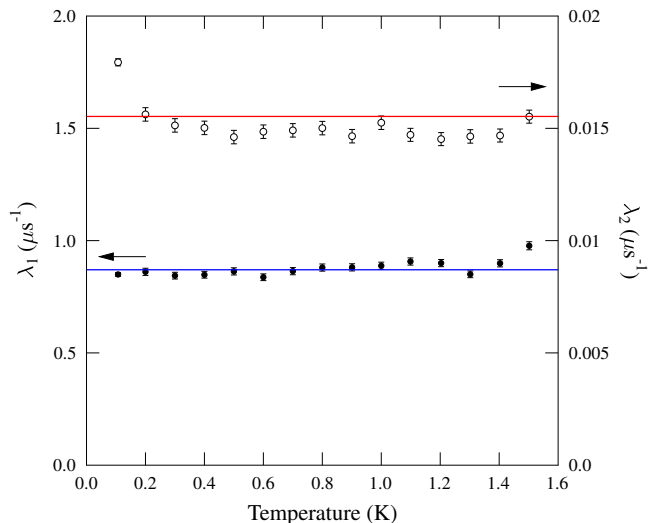


FIG. S4. Temperature dependence of the relaxation rates in Eq. 2. Both  $\lambda_1$  (filled circles) and  $\lambda_2$  (empty circles) are seen to be approximately constant. Note the different axis for each relaxation rate.

see that the effect of an applied LF is to quench the relaxation of the slowly-relaxing component of the asymmetry, which is likely to have a significant contribution from quasistatic nuclear moments. We also see that the amplitude of the faster-relaxing component is reduced. In order to examine the field-dependence of the faster relaxation rate, the spectra were fitted to

$$A(t) = A_{\text{rel}} e^{-\lambda t} + A_{\text{bg}}, \quad (5)$$

where the relaxing asymmetry  $A_{\text{rel}}$  reflects the dynam-

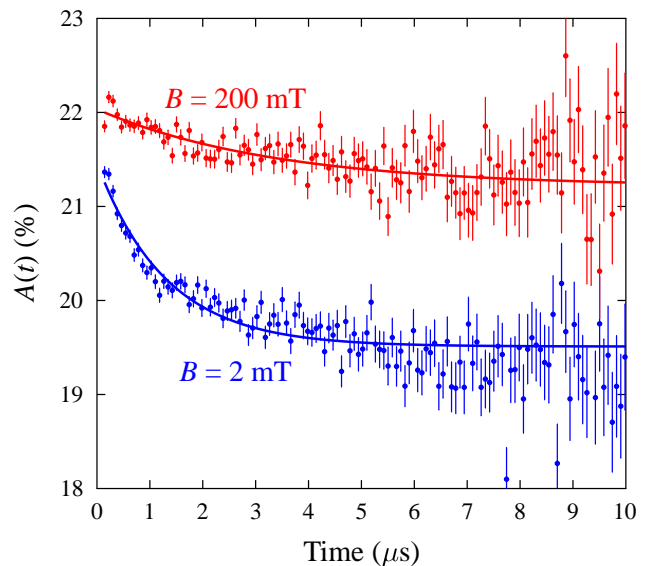


FIG. S5. Longitudinal field  $\mu^+$ SR spectra for  $\text{CuVOF}_4(\text{H}_2\text{O})_6 \cdot \text{H}_2\text{O}$  at two different fields. Spectra are displaced vertically for clarity.

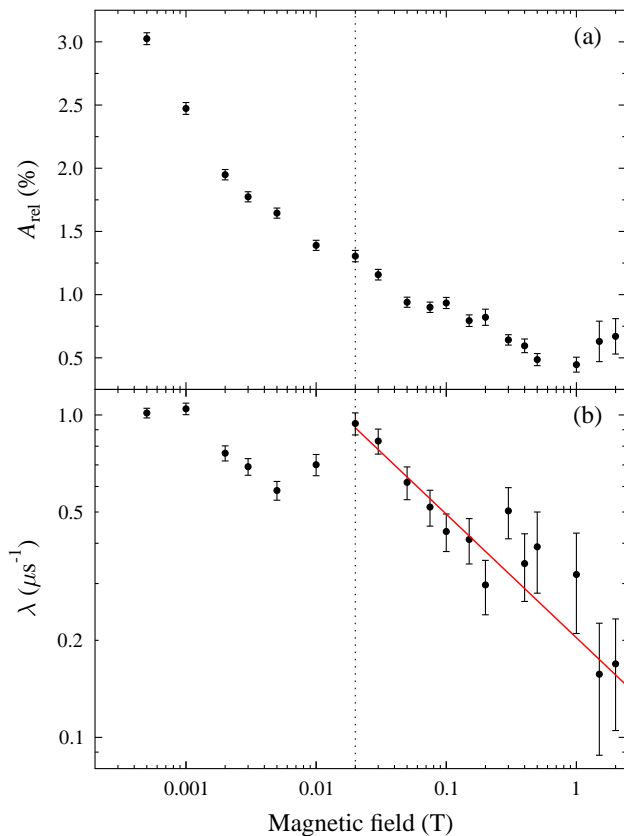


FIG. S6. (a) Relaxing asymmetry and (b) relaxation rate for  $\text{CuVOF}_4(\text{H}_2\text{O})_6 \cdot \text{H}_2\text{O}$  as a function of applied longitudinal magnetic field. In (b) we also show a fit to power law, appropriate for diffusive spin transport.

ics of the electron spins and  $A_{\text{bg}}$  represents a constant background asymmetry. The background asymmetry increases as a function of field, so was allowed to vary in the fits. The relaxing asymmetry  $A_{\text{rel}}$  [see Fig. S6(a)] and the relaxation rate  $\lambda$  [Fig. S6(b)] were both found to decrease with increasing field.

For fields below around 20 mT, the relaxation due to nuclear moments is not fully quenched and Eq. (4) provides a relatively poor fit to the data, with the residual nuclear relaxation influencing the values of  $\lambda$  obtained in these fits. The field-dependence of relaxing asymmetry is also particularly strong for these lower fields. On the other hand, for fields above 20 mT, the background relaxation is sufficiently quenched and Eq. (5) describes the spectra well. As shown in Fig. S6, the field-dependence of the relaxation rate is well-described by a power-law fit of the form  $\lambda = aB^{-n}$  with  $n = 0.38(4)$  for  $20 \leq B \leq 2000$  mT.

## Density functional theory

A commonly-used approach to calculating exchange constants using density functional theory involves computing the total energies of a series of spin configurations. The singlet-triplet gap  $J$  for two electrons can be obtained from the energy difference between the single-determinant broken symmetry (BS) and triplet (T) states via  $J = E_{\text{T}} - E_{\text{BS}}$  [10]. This approach can be extended to polynuclear systems by expressing the energy differences between different spin configurations as the sum of pairwise interactions [11]. The total energy for each configuration is then expressed in terms of an Ising model

$$E = \frac{1}{2} \sum_{i < j} J_{ij} \sigma_i \sigma_j + E_0, \quad (6)$$

where the Ising spin operators  $\sigma_{i,j} = \pm 1$  and  $E_0$  represents the nonmagnetic contribution to the total energy. This leads to a set of linear equations that can be solved to obtain the  $J_{ij}$  for each pair of spin centres.

We have used the DFT total energy approach to calculate the exchange constants corresponding to each of the exchange pathways in this system. The coupling constants  $J_{ij}$  assigned to each pair of spins for the structure in Fig. S7 are shown in Table. SII. These comprise an intradimer exchange  $J_0$  between Cu and V ion belonging to the same dimer, an interdimer exchange  $J''$  between Cu and V ions belonging to nearest-neighbour dimers within the  $bc$  plane and a further interdimer exchange  $J'$  between dimers along the  $a$  axis. By considering a ferromagnetic configuration and a series of antiferromagnetic configurations and mapping the DFT-calculated total energies to Eq. (6) we obtain the set of linear equations shown in Table SIII. We denote each spin configuration by a list of 0s (spin down) and 1s (spin up) in the order  $\text{Cu}_1\text{Cu}_2\text{Cu}_3\text{Cu}_4\text{V}_1\text{V}_2\text{V}_3\text{V}_4$ . By subtracting the total energies of pairs of configurations whose energies differ only by a sign in the coefficient multiplying the relevant

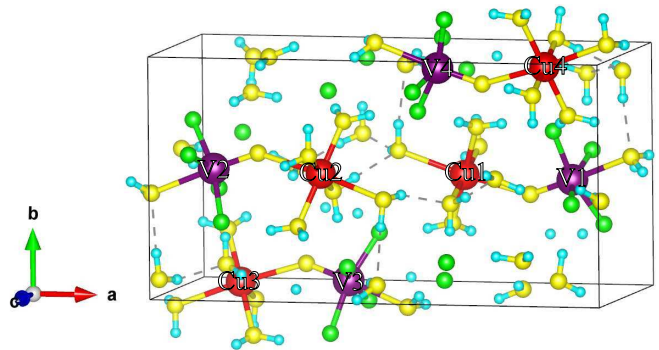


FIG. S7. Unit cell of  $\text{CuVOF}_4(\text{H}_2\text{O})_6 \cdot \text{H}_2\text{O}$  with labels corresponding to pairs of spins considered by Eq. 6 and as highlighted in Table SII.

Spin pair	$J_{ij}$
Cu1-V1	$J_0$
Cu1-V3	$J''$
Cu1-V4	$4J'$
Cu2-V2	$J_0$
Cu2-V3	$4J'$
Cu2-V4	$J''$
Cu3-V1	$J''$
Cu3-V2	$4J'$
Cu3-V3	$J_0$
Cu4-V1	$4J'$
Cu4-V2	$J''$
Cu4-V4	$J_0$

TABLE SII. Ising exchange constants assigned to each pair of spins in Eq. (6). We set  $J_{ij} = 0$  for all other pairs.

Spin configuration	Energy
11111111	$E_{\text{FM}} = 2J_0 + 8J' + 2J'' + E_0$
11110000	$E_{\text{AFM1}} = -2J_0 - 8J' - 2J'' + E_0$
11000011	$E_{\text{AFM2}} = -2J_0 + 8J' + 2J'' + E_0$
11001100	$E_{\text{AFM3}} = 2J_0 - 8J' - 2J'' + E_0$
10011001	$E_{\text{AFM4}} = 2J_0 + 8J' - 2J'' + E_0$
10010110	$E_{\text{AFM5}} = -2J_0 - 8J' + 2J'' + E_0$

TABLE SIII. Spin configurations and their associated energies given by Eq. (6).

exchange constant, we obtain the following expressions for the exchange constants,

$$\begin{aligned}
 J_0 &= \frac{E_{\text{AFM3}} - E_{\text{AFM1}}}{4}, \\
 J' &= \frac{E_{\text{AFM2}} - E_{\text{AFM5}}}{16}, \\
 J'' &= \frac{E_{\text{AFM4}} - E_{\text{FM}}}{4}.
 \end{aligned}
 \tag{7}$$

We note that these expressions are not unique, as Table SIII comprises a set of six linear equations containing only four independent variables, the three exchange constants  $J_0$ ,  $J'$  and  $J''$  and the nonmagnetic contribution to the total energy  $E_0$ . However, alternative expressions for  $J_0$  and  $J'$  yield values that agree with those obtained from Eq. 7 to within 10%. Magnetic exchange constants calculated using DFT can depend very strongly on the exchange-correlation functional employed [12]. The exchange constant  $J \sim t^2/U$  where  $t$  is the effective hopping integral and  $U$  is the onsite Coulomb interaction. Functionals such as the local spin density approximation and the generalized-gradient approximation (GGA) underestimate the localization (and hence  $U$ ) giving rise to an overestimate of  $J_0$  [12]. Hybrid functionals such as

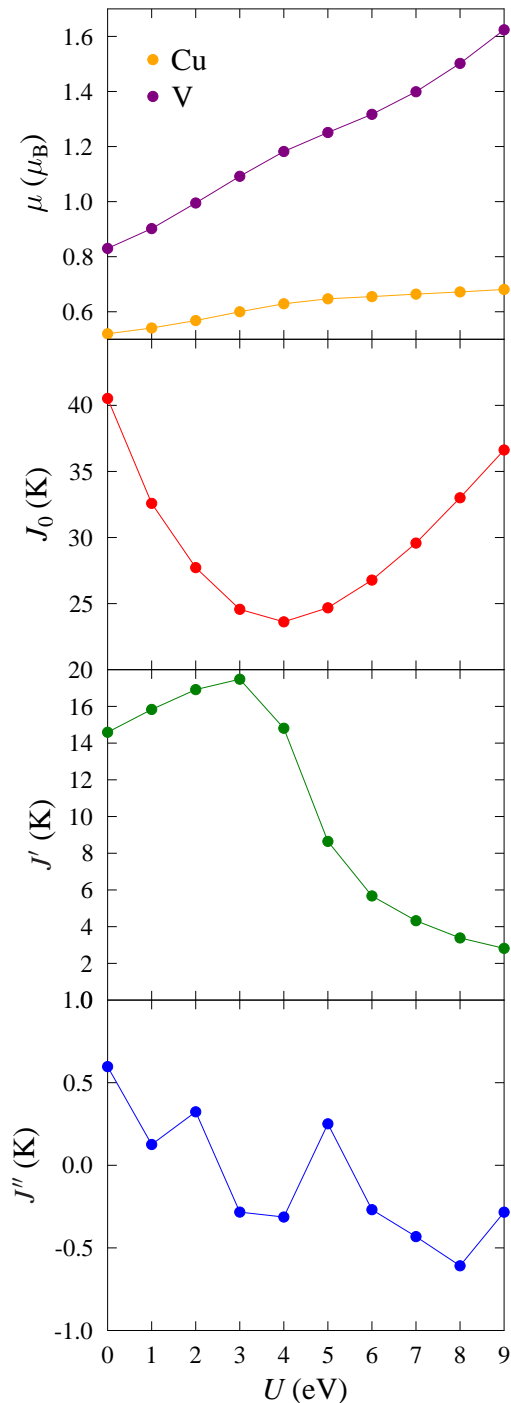


FIG. S8. Ordered moments and exchange constants as a function of the Hubbard  $U$  applied to both Cu and V  $d$  orbitals.

B3LYP can be used to remedy this in some cases and this approach has been applied successfully to number of Cu-based molecular magnets [13, 14]. Here, we instead using DFT+ $U$ , an extension to DFT where the strong onsite Coulomb interaction of localized electrons is treated with an additional Hubbard-like term. To determine the total energy associated with each of these magnetic struc-

tures, we carried out spin-polarised DFT+ $U$  calculations using the plane-wave basis-set electronic structure code CASTEP [15]. Calculations were carried out within the GGA using the PBE functional [16]. We used a plane-wave cutoff energy of 1400 eV and a  $1 \times 2 \times 2$  Monkhorst-Pack grid [17] for Brillouin zone integration, results in an energy difference between the FM and AFM1 configurations that converges to around 0.2 meV per unit cell. To account for the strong on-site Coulomb repulsion of localized electrons, a Hubbard  $U$  of equal magnitude was applied to both the Cu and V  $d$  orbitals. The calculated exchange constants and the magnitude of the ordered moments (obtained using population analysis) for each of the ions in the AFM1 configuration are shown in Fig. S8.

As seen in Fig. S8, the exchange constants depend very strongly on the value of  $U$  chosen. We also see that the moments on the magnetic ions increase with increasing  $U$ . This is especially true for V, whose moment increases by a factor of 2 between  $U = 0$  eV and  $U = 9$  eV. The principal exchange  $J_0$  initially decreases with increasing  $U$ , but reaches a minimum at  $U = 4$  eV and then recovers as  $U$  increases further. On the other hand, the interdimer exchange  $J'$  initially increases slightly with  $U$ , but for  $U > 3$  eV is rapidly suppressed with increasing  $U$ . The exchange constant  $J''$  is very small for all  $U$  and cannot be distinguished from zero within the uncertainties associated with these calculations. The principal exchange constant  $J_0 = 24.7(6)$  K obtained using  $U = 5$  eV shows reasonable agreement with the experiment result while also having a physically plausible value of  $U$ . The corresponding interdimer exchange constant  $J' = 8.6(15)$  K is somewhat larger than the experiment result. A value of  $J'$  can be obtained (at the expense of a larger  $J_0$ ) by going to larger values of  $U$ , but these are somewhat unphysical. The uncertainties in the calculated  $J_{ij}$  derives from limits on the convergence of the DFT energies with respect to the basis set [18]. We note that while the hybrid functional B3LYP has been shown to accurately predict the exchange constants in some other Cu-based systems, calculations using this functional on  $\text{Cu}(\text{H}_2\text{O})_5\text{VOF}_4 \cdot \text{H}_2\text{O}$  predict a ferromagnetic intradimer coupling, in clear contradiction with the experimental result.

The fact that both the intradimer and interdimer exchange constants are antiferromagnetic, i.e.  $J_0, J' > 0$  signifies that the configuration AFM1 is the ground state of the system. In Fig. 8 in the main text we show the spin density distribution for the ground state AFM1, obtained for  $U = 5$  eV (though we note that qualitatively similar results from  $U = 0$  eV). As seen in Fig. 8 in the main text, the spins of the Cu and V ions within a dimer are arranged antiferromagnetically, Cu and V spins belonging to neighboring dimers are also arranged antiferromagnetically. The spin density distribution across a single dimer when the system is in its magnetic ground state is shown in Fig. 8(b) in the main text. There is significant spin

density on the Cu and V ions; Mülliken population analysis shows that the total spin on the Cu and V ions is  $0.647 \hbar/2$  and  $1.251 \hbar/2$ , respectively. The O atom joining the Cu and V within a dimer has a total spin of  $0.234 \hbar/2$ , with this spin density having the opposite sign to the V ion within the dimer (this is also true for ferromagnetic dimer configurations). The Cu coordination octahedron experiences a Jahn-Teller (JT) distortion along the axis parallel to the Cu–O–V direction. This places the magnetic orbitals along the plane perpendicular to this axis, and we see this reflected in the shape of the isosurfaces of the spin density for the Cu ion. These orbitals lie along the Cu–O bonds and induces a total spin  $\approx 0.09 \hbar/2$  on each of the O atoms within this plane. (The combination of this delocalization of the Cu spin density across its coordination octahedron and the fact that the spin on central O atoms point in the opposite direction to the V spin means that the net spin for the whole system is close to zero, despite the greater spin density on the V ion compared to the Cu ion.) On the other hand, any spin density on the apical O atom on the outside of the dimer is very small. In light of this JT distortion and its effect on the spin density for O atoms along the JT axis, we should therefore consider the spin density on the O atom at the center of the dimer as instead resulting from an antiferromagnetic interaction with the V atom, with which it shares a short bond ( $\approx 1.6 \text{ \AA}$ ). The spin density on the F atoms is fairly small ( $< 0.01 \hbar/2$ ), which can be explained by the fact that the V–F bonds lie along nodes of the spin density on the V.

The spin density on the central O atom and its antiferromagnetic alignment with the spin of the V ion is likely to play a key role in promoting the intradimer exchange, though it is not clear how this exchange continues along the dimer to the Cu ion, given the fact that this O atom lies along the JT axis of Cu. The three-dimensional (3D) structure is built up by connecting these dimer units through  $\text{F} \cdots \text{H} - \text{O}$  hydrogen bonds. This pathway links O atoms in the JT plane, that are well-coupled to the Cu spin, to the F atoms bonded to the V spin and this gives rise to interdimer exchange  $J'$  and  $J''$ , within the  $bc$  plane and along the  $a$  axis, respectively. There are also hydrogen bonds between O atoms in the JT plane with apical O atoms on Cu ions in an adjacent dimer, but this exchange pathway might be expected to be weaker owing to the very small spin density on the apical O atom.

Spin-polarized band structures and density of states (DOS) for each of these magnetic configurations are shown in Fig. S9. For calculations of the density of states a finer  $5 \times 10 \times 10$  for Brillouin zone sampling was used. For all configurations the band structure is characterized by two sets of flat bands, one just above and just below the Fermi energy. The lack of significant band dispersion for these states implies that they are localized to the Cu and V. As seen from the projected density of states (PDOS) these correspond to the Cu and V ions,

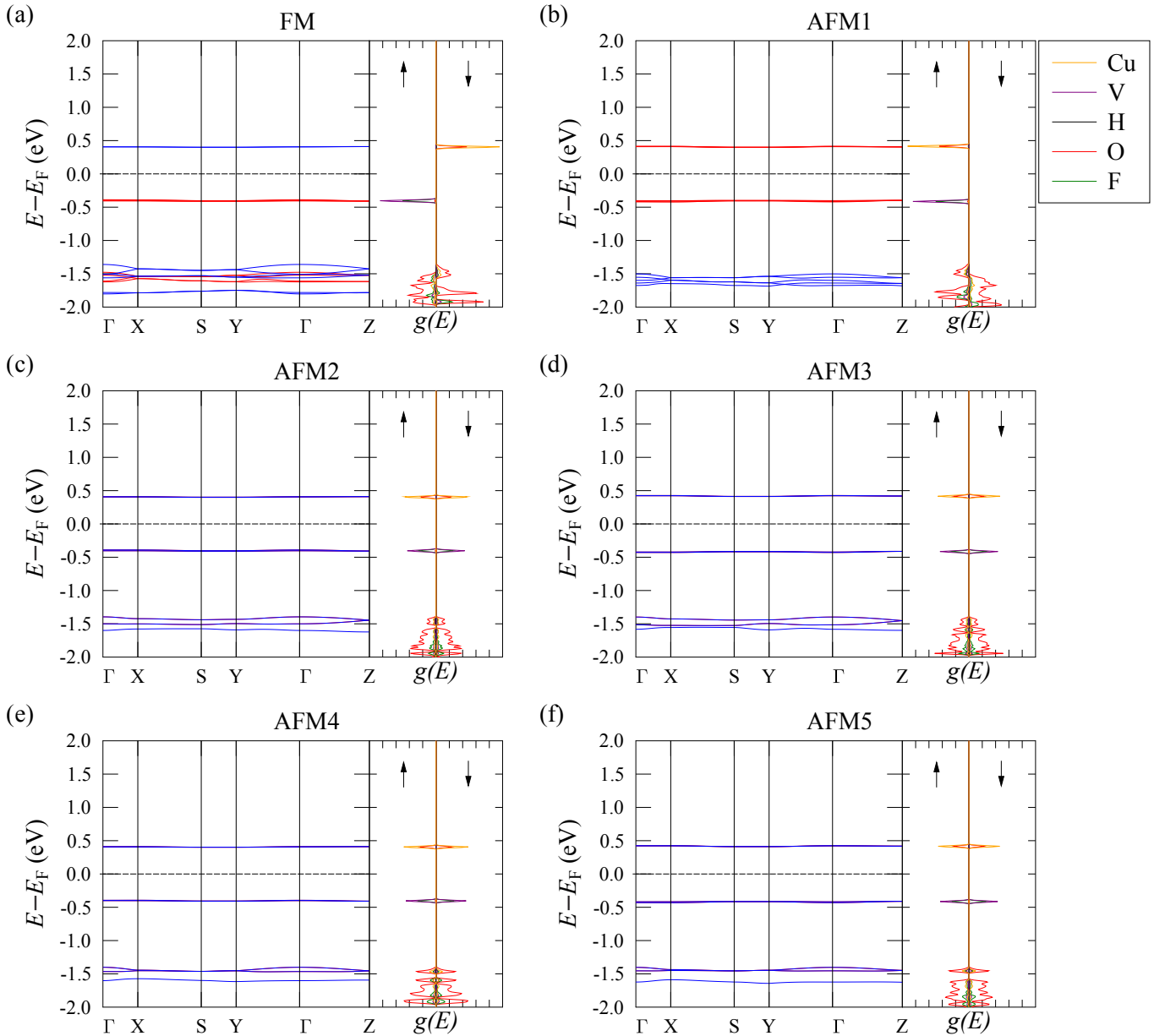


FIG. S9. Spin-polarized band structures for each of the magnetic configuration and the density of states for each spin channel. Bands corresponding to spin-up and spin-down are indicates by red and blue lines respectively. The density of states are shown projected onto atomic species.

respectively. The PDOS also show the hybridization between the Cu and V orbitals with those from O and F respectively. Note that these O atoms are those lying in the JT plane; the orbitals on both the apical and central O atoms along the JT axis instead lie further below the Fermi energy. For small values of  $U$ , these two sets of bands are sufficiently close to the Fermi energy ( $< 0.1$  eV away for  $U = 0$ ) that they are all fractionally occupied once smearing is taken into account. However, the band gap increases with increasing  $U$ , such that for  $U = 5$  eV the occupation of the bands above the Fermi energy is almost zero, with the bands below being close to fully

occupied.

The band structures and PDOS for configurations AFM2, AFM3, AFM4 and AFM5, shown in Figs. S9, are fairly typical for an antiferromagnetic system, with degenerate up and down bands and equal DOS in the up and down spin channels. For the FM state the Cu and V PDOS occupy opposite spin channels. The spin-up V orbitals are occupied and the spin-down Cu orbitals are unoccupied, resulting in an overall spin polarisation. For the AFM1 configuration the Cu and V PDOS instead occupy the same spin channel. This has an effect on which spin channel the Cu PDOS that lie well below the Fermi

energy (shown in Fig. 9 in the main text) occupy, such that the majority of occupied Cu orbitals are spin-down, giving an overall antiferromagnetic state.

### Tight-binding model

To more directly assess the relative strengths of the various exchange pathways we developed a description of the system in terms of a tight-binding model. To obtain an appropriate set of basis function we constructed maximally-localized Wannier functions [19, 20]. First-principles calculations were carried out using QUANTUM ESPRESSO [21, 22], with Wannier functions being computed using the interface with WANNIER90 [23]. As with our earlier calculations using CASTEP, these calculations were carried out within the GGA using the PBE functional [16]. To simplify our analysis, the system was treated as non-spin-polarized. Furthermore, values of the Hubbard  $U$  are generally not transferable, with their values depending on many physical or technical details (such as the pseudopotentials used), and hence the Hubbard  $U$  was omitted from these calculations. Pseudopotentials were obtained from the SSSP efficiency library [24], which specifies a projector-augment wave (PAW) pseudopotential for O [25], ultrasoft (US) pseudopotentials for F, V, and Cu [26], and an US pseudopotential for H [27]. Energy cutoffs of 60 Ry and 480 Ry were used for the wavefunctions and density, respectively, and  $3 \times 4 \times 5$  Monkhorst-Pack grid [17] was used for Brillouin zone sampling.

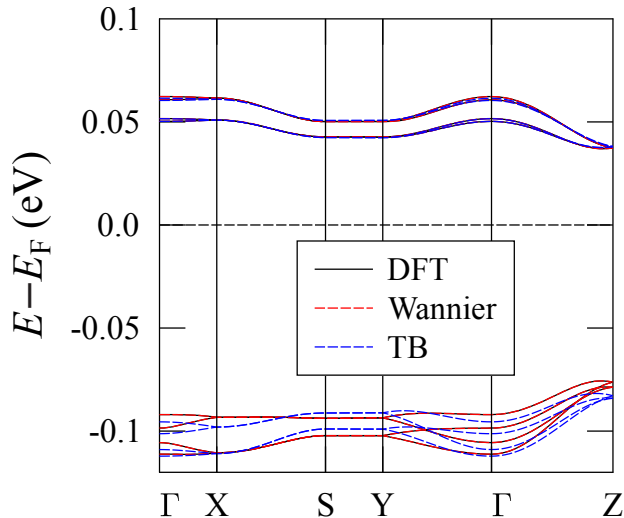


FIG. S10. Electronic band structures calculated using DFT (black solid line), a Wannier reconstruction (red dashed line) and a tight-binding model limited to nearest-neighbor hopping (blue dashed line).

The DFT band structure in the vicinity of the Fermi energy is shown in S10. It comprises two sets of four

bands, either  $\approx 0.05$  eV above or  $\approx 0.1$  eV below the Fermi energy and well-separated from the other bands. We note that due to the smearing employed in these calculations, the set of bands just above the Fermi energy are partially occupied. (The occupancies of the bands just below and above the Fermi energy are around 0.74 and 0.26, respectively). We therefore constructed a set of eight Wannier functions from the orbitals corresponding to these bands. The resulting Wannier functions are shown in Fig. S11, and fall into two distinct categories. These functions are either localized on Cu [Fig. S11(a)] or V [Fig. S11(b)]. There are four functions of each type, each localized on a different Cu or V ion within the unit cell.

We proceeded to construct a single-particle Hamiltonian using the set of Wannier orbitals  $|i\mathbf{R}\rangle$ , centered on the Cu or V ion  $i$  in the unit cell whose origin is at  $\mathbf{R}$ .

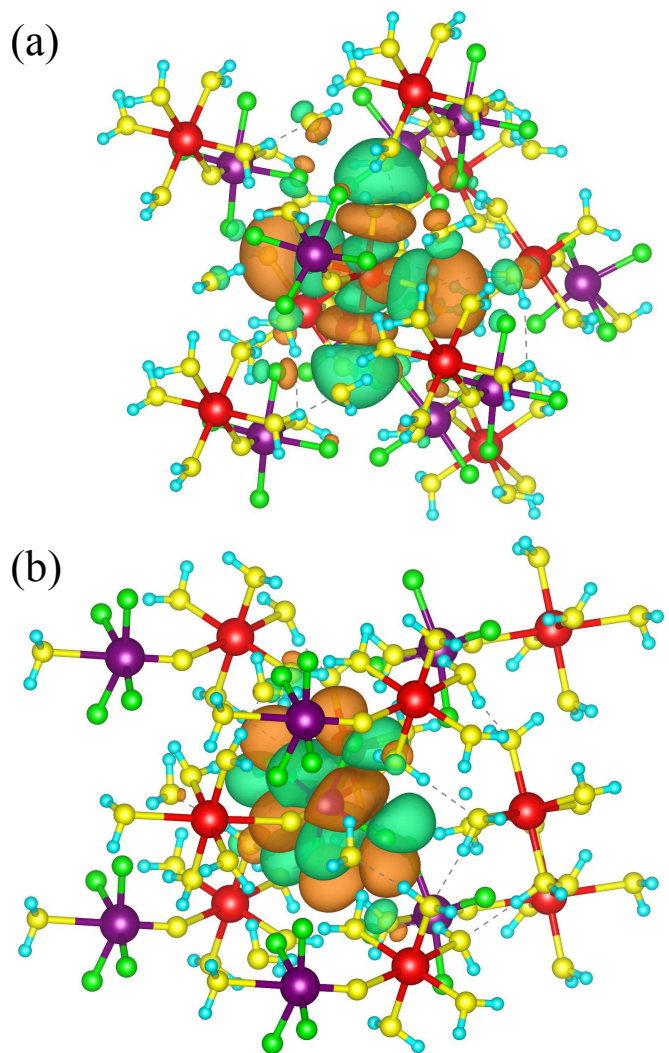


FIG. S11. The two distinct classes of maximally-localized Wannier functions, which are localized either on (a) Cu or (b) V.

The overlaps between the Wannier orbitals

$$h_{ij}(\mathbf{R}) = \langle i\mathbf{0} | \hat{\mathcal{H}} | j\mathbf{R} \rangle, \quad (8)$$

where  $\hat{\mathcal{H}}$  is the full microscopic Hamiltonian, lead to a model Hamiltonian

$$\hat{H} = \sum_{i,j,\mathbf{R}} \hat{c}_{i\mathbf{0}}^\dagger h_{ij}(\mathbf{R}) \hat{c}_{j\mathbf{R}}, \quad (9)$$

where  $\hat{c}_{j\mathbf{R}}^{(\dagger)}$  annihilates (creates) an electron at site  $j$  in the unit cell at  $\mathbf{R}$ . Diagonalizing  $\hat{H}$  yields the band structure shown as a red dashed line in Fig. S10. We see that the DFT band structure is reproduced accurately, demonstrating that the Wannier orbital construction was successful.

To assess the relative importance of the various exchange pathways, we constructed a tight-binding model based on Eq. 9, but limited to nearest-neighbor interac-

tions,

$$\hat{H}_{\text{TB}} = \sum_{i,j} \sum_{\{\mathbf{R}\}_{ij}} \hat{c}_{i\mathbf{0}}^\dagger h_{ij}(\{\mathbf{R}\}_{ij}) \hat{c}_{j\mathbf{R}}, \quad (10)$$

where the sum over lattice vectors is restricted to the set  $\{\mathbf{R}\}_{ij}$  for which  $|i\mathbf{0}\rangle$  and  $|j\mathbf{R}\rangle$  are centered on nearest-neighbor ions. Solving this model results in the band structure shown as a blue dashed line in Fig. S10. We see that while this model captures the main features of the band structure, its agreement with the DFT result is not as good as for the full Wannier reconstruction, which includes a significantly larger number of matrix elements  $h_{ij}(\mathbf{R})$ .

The evaluation of the hopping strength for a given exchange pathway is complicated by the fact that, for each pair of ions  $i$  and  $j$ ,  $h_{ij}(\{\mathbf{R}\}_{ij})$  can take more than one distinct value. This is due to the nearest-neighbor distances along different directions varying slightly, resulting in different overlaps. To simplify our analysis we define a hopping strength  $t_{ij}$  for each pair of ions as  $t_{ij} = \max\{h_{ij}(\mathbf{R}) : \mathbf{R}\}$ . Denoting each Wannier function by the ion at its center, we have in the basis (Cu1,Cu2,Cu3,Cu4,V1,V2,V3,V4),

$$\mathbf{t} = \begin{pmatrix} 0.01 & 0.63 & -0.41 & 1.53 & 2.87 & -0.21 & -5.20 & -25.28 \\ 0.63 & 0.01 & 1.53 & -0.41 & -0.21 & 2.87 & -25.28 & -5.20 \\ -0.41 & 1.53 & 0.01 & 0.63 & -5.20 & -25.28 & 2.87 & -0.21 \\ 1.53 & -0.41 & 0.63 & 0.01 & -25.28 & -5.20 & -0.21 & 2.87 \\ 2.87 & -0.21 & -5.20 & -25.28 & -0.79 & 0.76 & 0.06 & 0.61 \\ -0.21 & 2.87 & -25.28 & -5.20 & 0.76 & -0.79 & 0.61 & 0.06 \\ -5.20 & -25.28 & 2.87 & -0.21 & 0.06 & 0.61 & -0.79 & 0.76 \\ -25.28 & -5.20 & -0.21 & 2.87 & 0.61 & 0.06 & 0.76 & -0.79 \end{pmatrix} \text{meV}. \quad (11)$$

We first note that the hoppings between Cu ions (top-left quadrant) and between V ions (bottom-right quadrant) are generally smaller than those between Cu and V ions, justifying the omission of these exchange pathways from our earlier model for computing the exchange constants. For the hoppings resulting from the overlap between Cu and V ions, we can map these to the exchange constants calculated earlier, as these should be related via  $J \sim t^2/U$ . We find  $t = 2.87$  meV,  $t' = -25.28$  meV and  $t'' = -5.20$  meV, corresponding to  $J_0$ ,  $J'$  and  $J''$ , respectively. Immediately of note is the fact that, of these three transfer integrals, the one corresponding to the principal exchange  $J_0$  is actually the weakest. This can be rationalized by considering the shapes of the Wannier functions in Fig. S11. For both Cu- and V-centered Wannier functions, the wavefunctions are largest in the plane orthogonal to the intradimer direction, and hence their overlap within a dimer is small. On the other hand, the transfer

integral  $t'$  describing the overlap between these orbitals on adjacent dimers within the  $bc$  plane is much larger to the strong overlap for these directions. To obtain a transfer integral that more accurately reflects the interdimer exchange, we must consider that the interdimer coupling  $4J'$  is due to exchange between a Cu ion on a dimer and a V ion on each of four nearest-neighbour dimers. As noted above, these interdimer distances are not all equal and hence  $J'$  better represents the average coupling for exchange between dimers in the  $bc$  plane. We therefore consider all of the distinct transfer integrals corresponding to these pairs of Cu and V ions. These are  $t'_1 = -25.28$  meV,  $t'_2 = -21.64$  meV,  $t'_3 = -7.72$  meV,  $t'_4 = 1.45$  meV. Bearing in mind that  $J \propto t^2$  we can formulate an average hopping strength for interdimer coupling in the  $bc$  plane as

$$|t'_{\text{avg}}| = \sqrt{[(t'_1)^2 + (t'_2)^2 + (t'_3)^2 + (t'_4)^2]/4}. \quad (12)$$

The resulting effective hopping  $|t'_{\text{avg}}| = 17.1$  meV is still significantly larger than the intradimer hopping. We note that treating the system as spin-polarized instead produces nearly identical results to these, due to the fact that, in the magnetic ground state, the bands close to the Fermi energy all occupy the same spin channel.

---

\* [tom.lancaster@durham.ac.uk](mailto:tom.lancaster@durham.ac.uk)

† [jmanson@ewu.edu](mailto:jmanson@ewu.edu)

‡ [p.goddard@warwick.ac.uk](mailto:p.goddard@warwick.ac.uk)

- [1] Rigaku, <https://www.rigaku.com/products/crystallography/synergys>.
- [2] “Crysalispro,” CrysAlisPRO, Oxford Diffraction /Agilent Technologies UK Ltd, Yarnton, England.
- [3] G. M. Sheldrick, *Acta Crystallographica Section C* **71**, 3 (2015).
- [4] R. B. Clover and W. P. Wolf, *Rev. Sci. Instrum.* **41**, 617 (1970).
- [5] T. Coffey, Z. Bayindir, J. F. DeCarolis, M. Bennett, G. Esper, and C. C. Agosta, *Rev. Sci. Instrum.* **71**, 4600 (2000).
- [6] S. J. Blundell, *Contemporary Physics* **40**, 175 (1999).
- [7] S. Blundell, R. De Renzi, T. Lancaster, and F. Pratt, *Muon Spectroscopy: An Introduction* (Oxford University Press, 2021).
- [8] P. D. de Réotier and A. Yaouanc, *Journal of Physics: Condensed Matter* **9**, 9113 (1997).
- [9] R. S. Hayano, Y. J. Uemura, J. Imazato, N. Nishida, T. Yamazaki, and R. Kubo, *Phys. Rev. B* **20**, 850 (1979).
- [10] E. Ruiz, J. Cano, S. Alvarez, and P. Alemany, *Journal of Computational Chemistry* **20**, 1391 (1999).
- [11] E. Ruiz, A. Rodríguez-Fortea, J. Cano, S. Alvarez, and P. Alemany, *Journal of Computational Chemistry* **24**, 982 (2003).
- [12] R. L. Martin and F. Illas, *Phys. Rev. Lett.* **79**, 1539 (1997).
- [13] L. H. Dos Santos, A. Lanza, A. M. Barton, J. Brambleby, W. J. Blackmore, P. A. Goddard, F. Xiao, R. C. Williams, T. Lancaster, F. L. Pratt, S. J. Blundell, J. Singleton, J. L. Manson, and P. Macchi, *J. Am. Chem. Soc.* **138**, 2280 (2016).
- [14] B. M. Huddart, J. Brambleby, T. Lancaster, P. A. Goddard, F. Xiao, S. J. Blundell, F. L. Pratt, J. Singleton, P. Macchi, R. Scatena, A. M. Barton, and J. L. Manson, *Phys. Chem. Chem. Phys.* **21**, 1014 (2019).
- [15] S. J. Clark, M. D. Segall, C. J. Pickard, P. J. Hasnip, M. I. Probert, K. Refson, and M. C. Payne, *Zeitschrift für Krist.* **220**, 567 (2005).
- [16] J. P. Perdew, K. Burke, and M. Ernzerhof, *Phys. Rev. Lett.* **77**, 3865 (1996).
- [17] H. J. Monkhorst and J. D. Pack, *Phys. Rev. B* **13**, 5188 (1976).
- [18] I. O. Thomas, S. J. Clark, and T. Lancaster, *Phys. Rev. B* **96**, 094403 (2017).
- [19] N. Marzari and D. Vanderbilt, *Phys. Rev. B* **56**, 12847 (1997).
- [20] I. Souza, N. Marzari, and D. Vanderbilt, *Phys. Rev. B* **65**, 035109 (2001).
- [21] P. Giannozzi, S. Baroni, N. Bonini, M. Calandra, R. Car, C. Cavazzoni, D. Ceresoli, G. L. Chiarotti, M. Cococcioni, I. Dabo, A. D. Corso, S. de Gironcoli, S. Fabris, G. Fratesi, R. Gebauer, U. Gerstmann, C. Gougoussis, A. Kokalj, M. Lazzeri, L. Martin-Samos, N. Marzari, F. Mauri, R. Mazzarello, S. Paolini, A. Pasquarello, L. Paulatto, C. Sbraccia, S. Scandolo, G. Sclauzero, A. P. Seitsonen, A. Smogunov, P. Umari, and R. M. Wentzcovitch, *Journal of Physics: Condensed Matter* **21**, 395502 (2009).
- [22] P. Giannozzi, O. Andreussi, T. Brumme, O. Bunau, M. B. Nardelli, M. Calandra, R. Car, C. Cavazzoni, D. Ceresoli, M. Cococcioni, N. Colonna, I. Carnimeo, A. D. Corso, S. de Gironcoli, P. Delugas, R. A. DiStasio, A. Ferretti, A. Floris, G. Fratesi, G. Fugallo, R. Gebauer, U. Gerstmann, F. Giustino, T. Gorni, J. Jia, M. Kawamura, H.-Y. Ko, A. Kokalj, E. Küçükbenli, M. Lazzeri, M. Marsili, N. Marzari, F. Mauri, N. L. Nguyen, H.-V. Nguyen, A. O. de-la Roza, L. Paulatto, S. Poncé, D. Rocca, R. Sabatini, B. Santra, M. Schlipf, A. P. Seitsonen, A. Smogunov, I. Timrov, T. Thonhauser, P. Umari, N. Vast, X. Wu, and S. Baroni, *Journal of Physics: Condensed Matter* **29**, 465901 (2017).
- [23] G. Pizzi, V. Vitale, R. Arita, S. Blügel, F. Freimuth, G. Géranton, M. Gibertini, D. Gresch, C. Johnson, T. Koretsune, J. Ibañez-Azpiroz, H. Lee, J.-M. Lihm, D. Marchand, A. Marrazzo, Y. Mokrousov, J. I. Mustafa, Y. Nohara, Y. Nomura, L. Paulatto, S. Poncé, T. Ponweiser, J. Qiao, F. Thöle, S. S. Tsirkin, M. Wierzbowska, N. Marzari, D. Vanderbilt, I. Souza, A. A. Mostofi, and J. R. Yates, *Journal of Physics: Condensed Matter* **32**, 165902 (2020).
- [24] G. Prandini, A. Marrazzo, I. E. Castelli, N. Mounet, and N. Marzari, *npj Computational Materials* **4**, 72 (2018).
- [25] E. Kucukbenli, M. Monni, B. I. Adetunji, X. Ge, G. A. Adebayo, N. Marzari, S. de Gironcoli, and A. D. Corso, “Projector augmented-wave and all-electron calculations across the periodic table: a comparison of structural and energetic properties,” (2014), [arXiv:1404.3015 \[cond-mat.mtrl-sci\]](https://arxiv.org/abs/1404.3015).
- [26] K. F. Garrity, J. W. Bennett, K. M. Rabe, and D. Vanderbilt, *Computational Materials Science* **81**, 446 (2014).
- [27] A. Dal Corso, *Computational Materials Science* **95**, 337 (2014).